Thermal shock of tungsten carbide in plasma-facing conditions

S.A. Humphry-Baker [a,1], G.D.W. Smith [b], and G. Pintsuk [c]
[a] *Imperial College London, London, SW7 1AZ, UK*
[b] *Tokamak Energy Ltd, Abingdon, OX14 4SD, UK*
[c] *Forschungszentrum Juelich GmbH, 52428 Juelich, Germany*

Abstract

Tungsten carbide (WC) has been found to have higher resistance to plasma-induced thermal-shock compared to rolled tungsten. The electron beam device JUDITH 1 was used to simulate likely thermal shock conditions induced by edge localised modes and plasma disruptions. Loading conditions of 100-1000 cycles, heat fluxes of 0.19-1.13 GW/m^2 and base temperatures of 400-1000 °C were employed on two candidate WC-based materials: a monolithic WC ceramic, and a WC-FeCr composite. Surprisingly, the monolith outperformed the composite under all conditions. This was unexpected, particularly at low temperature, based on the calculated thermal shock resistance parameters. The result was explained by preferential melting of the metallic FeCr binder. Compared to available data collected under identical conditions on rolled tungsten plate, WC had lower surface roughness from thermal shock damage, particularly when tested at 400 °C. This shows promise for using WC as a plasma facing material; strategies for further improving performance are discussed.

Keywords: tungsten carbide, thermal shock, plasma-facing, high heat flux.

1. Introduction

Plasma facing materials in fusion reactors will experience extreme thermal environments. In addition to expected steady state heat fluxes, such as ~10 MW/m^2 in the strike point region of the divertor, more intense transient heating events will be experienced. Examples of these include edge localised modes (ELMs) and plasma disruptions. During an unmitigated ELM occurring with a frequency of ~1 Hz during H-mode operation, transient heat fluxes may reach 1-10 GW/m^2 for durations of ~0.5 ms [1]. Events like plasma disruptions may deposit even larger heat fluxes over longer durations in the range of up to 10 ms and are high risk off-normal events. Plasma disruptions could lead to significant surface melting and erosion and must be avoided as much as possible. On the other hand, ELMs will inevitably, depending on the applied load and frequency, lead to the accumulation of surface damage by thermal fatigue. The mechanisms of such damage include plastic deformation, surface cracking and localised melting, which may cause significant erosion, material migration around the torus, and dissemination of matter into the plasma.

Recent efforts to characterise damage from such thermal shock events have focussed on metallic tungsten and its alloys, which are the primary candidate plasma-facing materials [2–8]. Tungsten's advantages are its high thermal conductivity and melting point, however its low temperature brittleness and relatively low fracture toughness mean that it is susceptible to extensive thermal stress-induced crack formation – even after a single pulse [8]. In multi-pulse loading, the crack morphology is heavily influenced by microstructure. In rolled tungsten plate, where the grain network is highly textured, the orientation of the long-axes of

[1] Corresponding author: shumphry@ic.ac.uk; +447801 555864

the grains relative to the thermally exposed surface plays a key role [3–5]. When these axes are within the surface, the in-plane mechanical properties are enhanced, leading to a higher power threshold for crack formation [3–5]. These textured, deformation-processed materials are also susceptible to recrystallisation, which leads to a significant decrease in thermal shock resistance [2–6]. A successful method for improving the shock performance of tungsten has been to alloy it with a fine dispersion of ceramic particles such as Y_2O_3 [9] or TiC [10]. Such dispersions generally refine the grain size and thus increase the material's fracture strength. They also have a secondary benefit of increasing the recrystallisation temperature. Thus, when such dispersions are introduced in the optimum quantity and size range, the overall thermal shock resistance of tungsten can be enhanced [9].

The aim of this work was to explore an alternative way to improve thermal shock performance of plasma facing materials by employing an Ultra-High Temperature Ceramic (UHTC) as the major constituent. The advantages of UHTCs include high melting points (~3000 °C and above), high thermal conductivity and phase stability [11]. Additionally, their ordered structure leads to an intrinsically high resistance to dislocation motion compared to refractory metals such as tungsten. As a result, they retain impressive strength at very high temperatures, e.g. ZrB_2-based materials have displayed flexural strengths of ~300 MPa at 2200 °C [12]. The UHTC tungsten carbide could be a promising plasma-facing material because of its combination of the above properties. The properties relating to the generic materials challenges for fusion, such as heat flux, irradiation, and hydrogen interaction, were recently reviewed [13]. The performance of WC in a simulated plasma facing environment remains unexplored. In this study, two candidate WC-based materials were thermal-shock tested: a monolithic WC ceramic, and a WC-FeCr composite. The composite material was selected on the basis of its higher fracture toughness. Somewhat unexpectedly, the monolith outperformed the composite, which was attributed to melting of the composite's metallic binder and loss of strength at high temperature. Compared to available data on industrial-grade rolled tungsten, the WC monolith had a lower surface roughness after thermal shock, which could be indicative of its higher resistance to crack formation.

2. Material and Methods

The monolithic WC material was manufactured by Plansee Composite Materials GmbH by spark plasma sintering at 2000 °C with an applied compressive stress of ~30 MPa. Fig. 1(a) is an electron back-scatter diffraction (EBSD) image, determined using taken using a Zeiss Sigma 300 scanning electron microscope (SEM) equipped with an Oxford Instruments HKL eFlash EBSD detector. The material had a grain size of 0.52 ± 0.07 μm as determined by the linear intercept grain size method. The WC-FeCr material was manufactured by Sandvik Hyperion Ltd. It was vacuum sintered at ~1450 °C. Fig. 1(b) shows the grain structure, as imaged on a LEO Gemini 1525 Field Emission Gun SEM. The material had a linear intercept grain size of 0.78 ± 0.46 μm.

Flexural strength was determined on 3x4x25 mm specimens, ground to a 1200 grit finish, with a chamfer of ~0.1 mm on each corner to minimise stress concentrations. The load was applied via graphite push rods in a 3-point bending geometry with a load span of 20 mm and a crosshead speed of 0.5 mm/min. Samples were heated under vacuum in a tungsten element furnace to 400 and 1000 °C. Four samples of each material were tested at each temperature, apart from WC-FeCr at 1000 °C, which failed after extensive plastic deformation. Table 1 shows that the flexural strength of each material varied with temperature differently: At 400 °C, WC-FeCr has a ~50% higher strength than WC. At 1000 °C, the trend is reversed, with WC-FeCr showing the lower strength by a factor of 3.

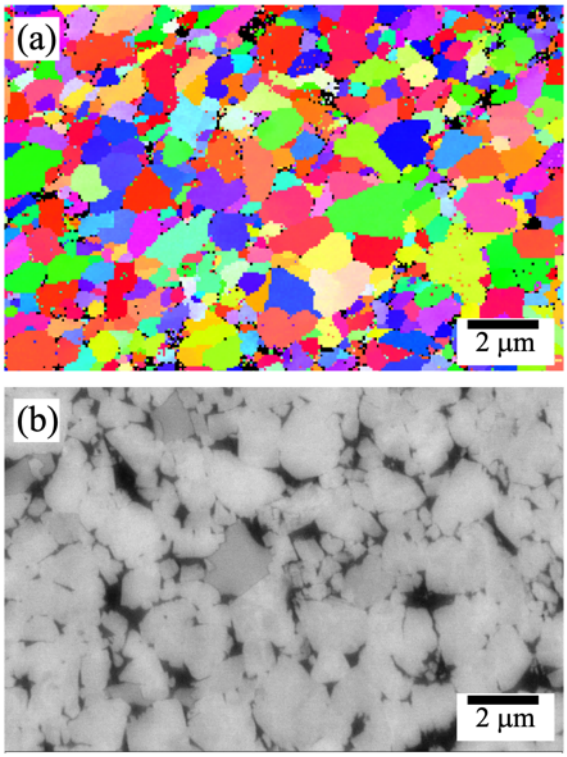

Fig. 1. (a) EBSD image of pure WC. (b) SEM micrograph of WC-FeCr showing WC particles in light contrast and FeCr binder in dark.

Thermal conductivity of monolithic WC was determined by measuring the diffusivity of 12.7 mm diameter disks using the laser flash method on a Netzsch LFA 427 analyser operated in flowing argon with a laser pulse of 600 V for 0.8 ms. Specific heat and temperature-dependent theoretical density were taken from [14]. The relative density was determined using the Archimedes method to be 98.8 %. WC-FeCr thermal conductivity data was taken from a previous study [15]. Table 1 shows the thermal conductivity of WC was about 15-20 % higher than WC-FeCr.

Table 1

Flexural strength, σ_f and thermal conductivity, k of each material. The uncertainty in σ_f represents the standard deviation on four repeat measurements.

material	σ_f $^{400\ °C}$ (GPa)	σ_f $^{1000\ °C}$ (GPa)	k $^{400\ °C}$ (W/m-K)	k $^{1000\ °C}$ (W/m-K)
WC	1.16 ± 0.22	1.84 ± 0.07	81	63
WC-FeCr	1.72 ± 0.24	0.61	70	53

For thermal shock tests, specimens of dimensions 12x12x5 mm^3 were polished to a mirror finish using 50 nm colloidal silica suspension as the final step. Tests were performed using the electron beam device JUDITH 1. Conditions were selected based on previous studies on tungsten [3,4] to allow for comparison and are listed in Table 2. To simulate ELMs, samples were pulsed at power densities of 0.19, 0.28 and 0.38 GW/m^2 for 1000 pulses of 1 ms duration at 1000 °C (labelled EL, EM, and EH – for low, medium, and high power respectively). To investigate the effect of temperature, the EH experiment was replicated at a base temperature of 400 °C (labelled EH-lt). To simulate disruption events, samples were pulsed at 1.13 GW/m^2 for 100 pulses of 5 ms duration (labelled DE). This energy was selected to be in excess of the power density for melting of W, which is ~0.88 GW/m^2 [6]. The exposed area of the sample in all tests was 4x4 mm and the repetition frequency was

<0.5 Hz to allow for the sample to cool between pulses. After thermal shock, the samples were characterised using SEM. The crack spacing was determined using the linear intercept method and the crack width was taken from the average of the 5 largest cracks observed. The arithmetic mean surface roughness was determined using laser profilometry.

Table 2
Loading temperature, T, power, P, pulse number, n and pulse time, Δt, for each condition.

condition	T (°C)	P (GW/m^2)	n (#)	Δt (ms)
EL	1000	0.19	1000	1
EM	1000	0.28	1000	1
EH	1000	0.38	1000	1
EH-lt	400	0.38	1000	1
VDE	1000	1.13	100	5

3. Results

3.1. ELM simulations

Fig. 2 shows the effect of the power density on the surface damage of WC-FeCr at 1000 °C. Figs. 2(a-c) show an overview of the crack network formation. As the power increases, the maximum crack width increases from about 10 μm for the 0.19 GW/m^2 sample, to about 50 μm at 0.38 GW/m^2. The high magnification images, Figs. 2(d-f), show differences in the fracture surfaces. The 0.19 GW/m^2 image shows a jagged surface, with facetted WC particles. The 0.28 and 0.38 GW/m^2 images show smoother surfaces with no visible particles. Accompanying the evolution of a smooth surface is a significant increase in density of small (20-50 nm) spherical pores, indicated by triangles. Such pores are not observed in cross sections of the as-received material, e.g. Fig. 1. Their spherical nature indicates that they form from a liquid phase. This, combined with the onset of smoothing of the fracture surface, suggests that melting occurred during the ELM simulations and that the degree of melting increases significantly between 0.19 and higher power densities.

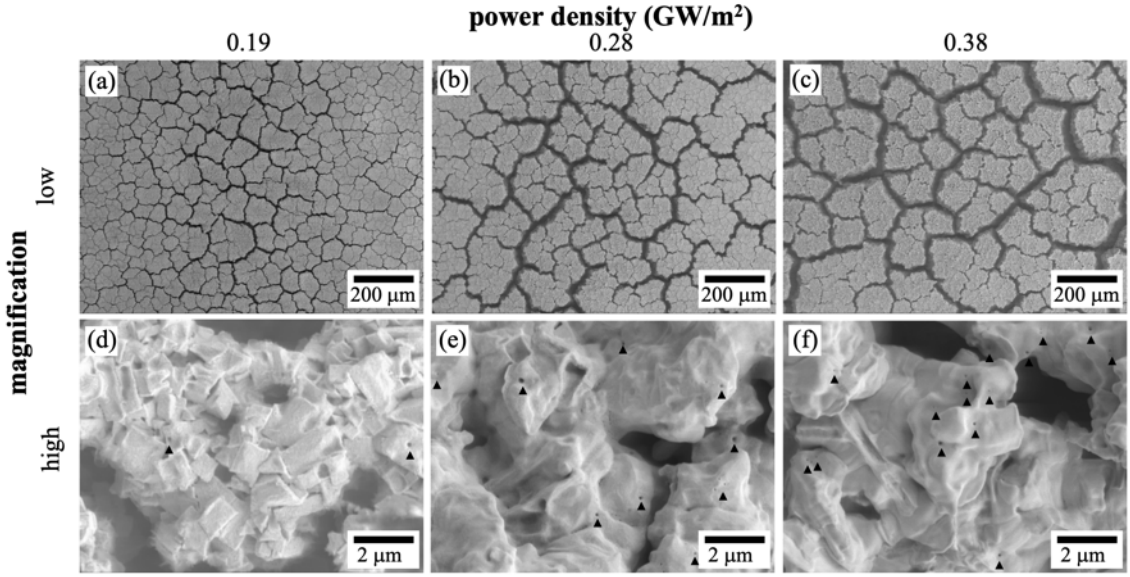

Fig. 2. (a-c) low magnification SEM images of WC-FeCr after thermal shock at 1000°C for 1000 cycles showing extensive crack networks. (d-f) high magnification micrographs showing that the density of bubbles on the surface (indicated by triangles) increases with increasing power density.

Fig. 3 shows the surface damage on monolithic WC after being exposed to the same ELM simulation conditions at 1000 °C. The Figs. 3(a-c) show the crack networks, which are narrower and less closely spaced than for WC-FeCr. The crack widths are between 0.5 μm and 5 μm (for 0.19 and 0.38 GW/m^2 respectively), which is a factor of 10 lower than WC-FeCr. The high magnification images show mostly similar surface morphologies, with one minor difference: In the 0.19 and 0.28 GW/m^2 samples, grain boundary grooves are visible on the surface. In the 0.38 GW/m^2 sample, the grain boundary grooves are masked by trans-granular striations, which are indicative of significant plastic deformation. Unlike WC-FeCr, none of the surfaces show any evidence of liquid phase formation.

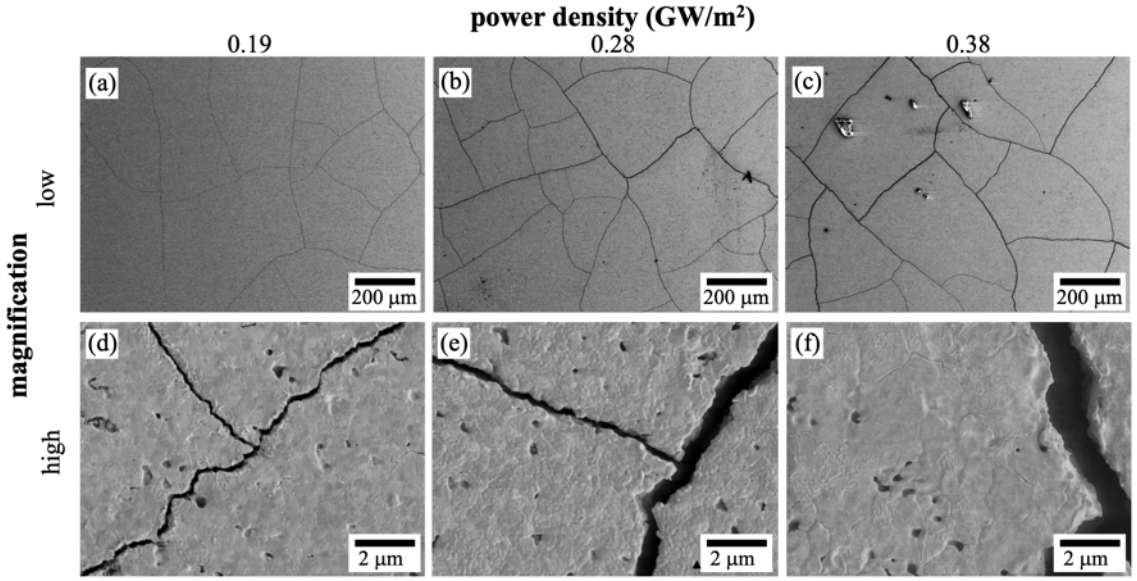

Fig. 3. (a-c) low magnification SEM images of monolithic WC after thermal shock at 1000°C for 1000 cycles. Cracking is less severe than for WC-FeCr. (d-f) high magnification micrographs showing grain boundary grooving and, at 0.38 GW/m^2, intragranular striations.

Fig. 4 shows cross-sectional images of the crack networks formed in WC and WC-FeCr at 0.38 GW/m^2, i.e. the view perpendicular to Figs. 2(c) and 3(c). In WC-FeCr, shown in part (a), there are clearly two distinguishable crack populations: large macro-cracks that extend ~200 μm into the depth, and smaller, micro-cracks that extend only ~20 μm. There is also extensive void formation in the cracked region, particularly localised at the maximum crack depth. In some areas these voids are so extensive that two neighbouring cracks connect. Thus, it appears the cracks grow parallel to the surface, at least partially, by void coalescence. In the monolithic WC, shown in part (b), there are no such micro-cracks, with only larger cracks that extend >200 μm into the depth. The deeper crack penetration is indicative of the comparatively brittle nature of WC compared to the WC-FeCr.

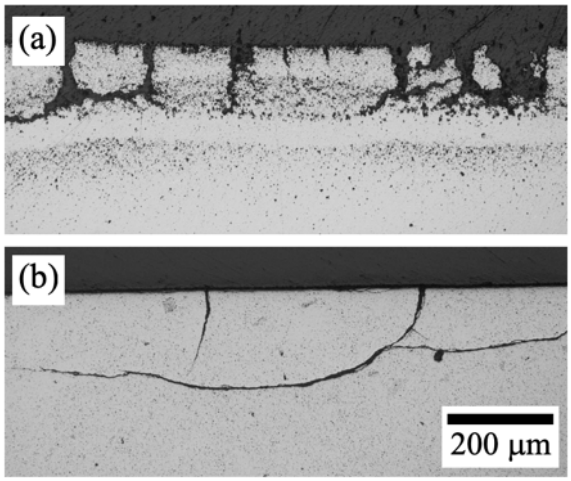

Fig. 4. cross-sectional SEM images of (a) WC-FeCr and (b) monolithic WC after 0.38 GW/m^2 thermal shock at 1000°C for 1000 cycles.

Fig. 5 shows the surface damage on both materials after the low temperature (400 °C) ELM simulations. Compared to the same power density tests at 1000 °C (i.e. Figs. 2c and 3c), the crack spacing in both materials is finer and the individual crack widths are narrower. Also in agreement with Figs. 2-3, the WC-FeCr crack separation is finer compared to WC and the crack width is a factor of ~10 greater. The high magnification images, which are not shown here for brevity, showed very similar behaviour to those in Figs. 2(f) and 3(f). That is, the extensive nanoscale bubble formation is seen for the WC-FeCr material, indicative of localised melting of the FeCr binder. Similarly, there were intragranular damage striations on the monolithic WC.

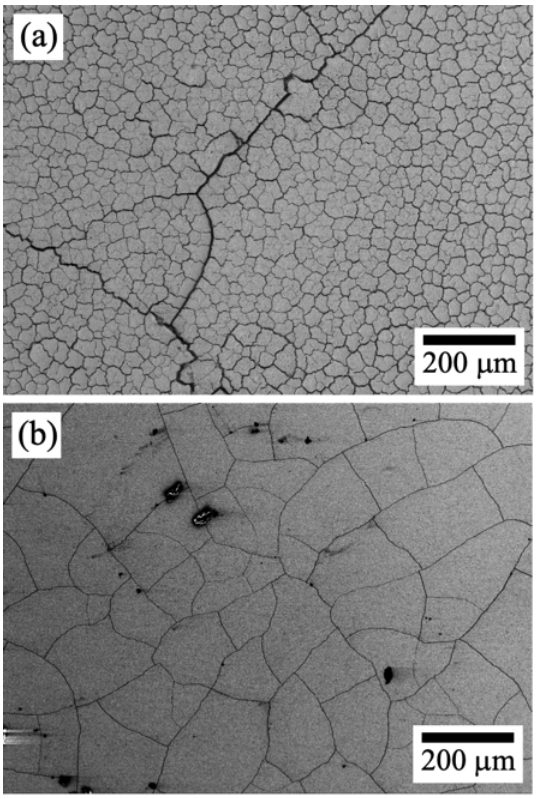

Fig. 5. low magnification SEM micrographs of (a) WC-FeCr and (b) monolithic WC after thermal shock at 400°C for 1000 cycles. In both cases, a finer array of narrower cracks is observed compared to the same test at 1000°C.

Fig. 6 summarises the surface roughness, crack spacing, and crack width, of both materials after ELM exposure. In accordance with the extensive damage in WC-FeCr, as shown in Figs. 2-5, the composite shows higher surface roughness, larger crack width, and closer crack spacing than WC, at all levels of power density and temperature. Fig. 6 also shows that at lower temperatures, i.e. at 400 °C, both materials show lower surface roughness, with more closely spaced cracks of finer widths compared to the same power density tests at 1000 °C.

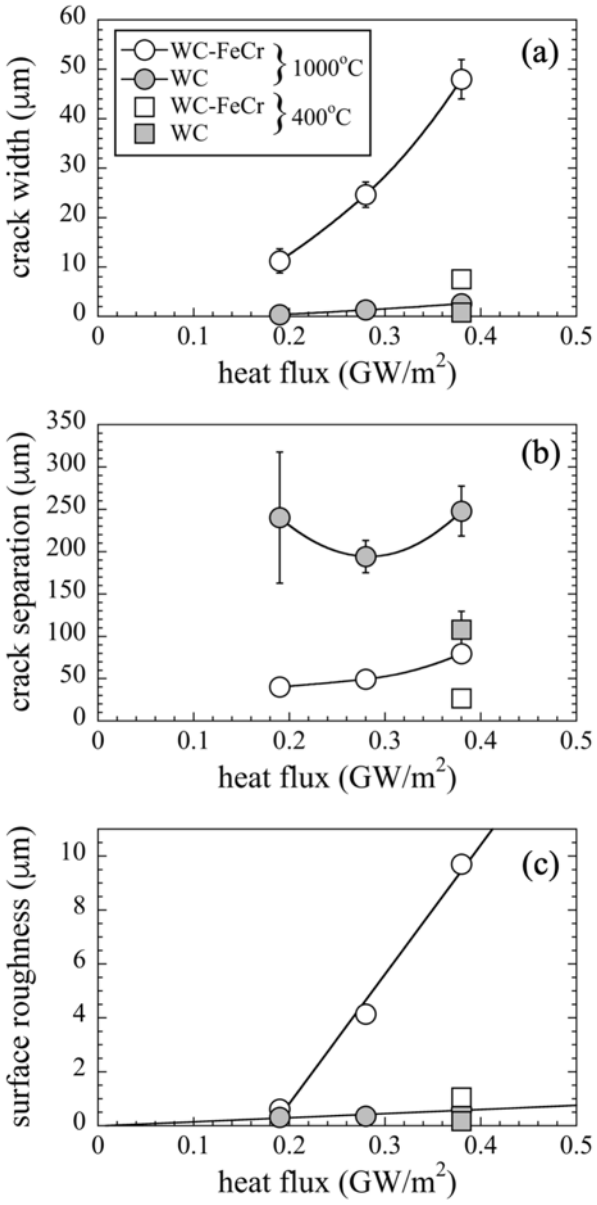

Fig. 6. crack width (a), crack separation (b) and surface roughness (c) of WC-FeCr (open symbols) and monolithic WC (closed) at 400 °C and 1000 °C as a function of power density. A linear fit for the WC-FeCr intersects the x-axis at 0.18 GW/m^2, taken as the threshold for damage.

The crack width, crack separation, and surface roughness tended to increase monotonically with increasing heat flux. The crack separation for WC was the exception to the rule; between 0.19 and 0.28 GW/m^2 it decreased with heat flux. This can be explained by the fact that at 0.19 GW/m^2 the crack network did not extend throughout the entire exposed area, i.e. in some areas of the exposed region no cracking was seen.

The surface roughness values can be considered as a measure of the overall degree of damage: Both 1000 °C data series are reasonably well-fit with a linear trendline with energy. The trendlines for WC and WC-FeCr show different behaviour: while the WC line of best fit intersects with the x-axis at a power density of 0, the WC-FeCr one intersects at a heat flux of 0.18 GW/m^2. This suggests there may be some measurable threshold for damage in this material. The observations of liquid formation in Fig. 2, suggests that this threshold power density could be that for liquid phase formation.

3.2. Disruption events

Fig. 7(a-b) shows the WC-FeCr sample after the disruption event simulation. Part (a) is a top-down view of the sample, showing extensive depressions and protrusions in the centre of the sample. There was no network of surface cracks, and the resulting surface roughness value was 7.7 μm, which was lower than the surface roughness of the highest power density ELM sample, 9.7 μm. The comparative lack of crack network and relatively smooth surface suggests that the surface material melted on a macroscopic scale and flowed as a liquid. Part (b) is a cross-section of the same area, showing a depression of the surface by ~0.5 mm, indicating significant loss of material. Also shown is a thick layer of darker material, ~0.1 mm in thickness. The darker contrast indicates this layer is rich in carbon and poor in metallic species. This observation, coupled with the loss of material, suggests that extensive loss of Fe and Cr, and possibly W has occurred, presumably through volatilisation from the liquid phase. Fig. 7(c-d) shows the corresponding damage on the WC sample after the same treatment. Part (c), the top-down view, shows a large crack running through the heat affected region. The surface roughness value of 2.9 μm is far in excess of any of the ELM simulated samples. In addition, there was significant discoloration in the heat affected region, indicating that the surface is carbon rich. The cross-section shown in part (d) shows a relatively flat surface, with a minor amount of material removal. The central region is covered in a layer of dark, presumably carbon rich material, beneath which an extensive crack network extends 200-400 μm into the material, mostly parallel to the surface.

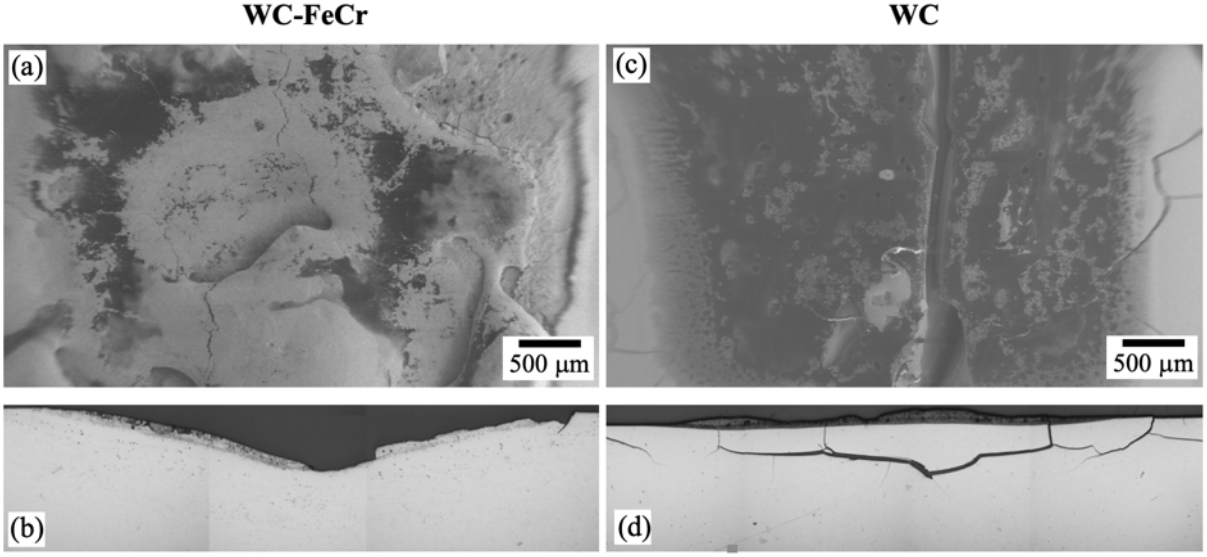

Fig. 7. (a-b) plasma disruption on WC-FeCr, (a) top-down view showing extensive liquid formation; (b) cross section showing loss of material. Part (c-d) view of WC monolith, (c) top-down view showing formation of carbon-rich region; (d) cross section showing minor recession of the surface.

4. Discussion

The most unexpected aspect of this work was the enhanced performance of WC compared to WC-FeCr. The reasons for this are first discussed by correlating the damage levels with calculated thermal shock parameter. Because this parameter does not capture the physics of melting, we secondly calculate the peak temperature profiles during each shock treatment, to understand the conditions under which melting occurs. The discussion ends with a comparison of the shock performance of WC with the leading candidate plasma facing material, metallic tungsten.

4.1. Thermal shock parameters

A material's resistance to thermal shock damage is usually characterised by its thermal shock parameter, *R*. The variant of this parameter relevant to the maximum allowable heat flux before failure is given by [16]:

$$R = \frac{k(1-\nu)\sigma_f}{E\alpha} \quad (1)$$

Where E is the Young's modulus, ν is the Poisson's ratio and α is the linear thermal expansion coefficient. Table 3 shows values of these parameters for each material at each set-point temperature, except for σ_f and k, which were given previously in Table 1. The WC data are taken from [14], while data for WC-FeCr are calculated as follows: The modulus is estimated by combining data from [14] with the temperature dependence of Fe taken from [17]. From these, the modulus of the composite is then calculated using the analytical expression given by Ravichandran [18]. The Poisson's ratio is calculated from the Poisson's ratios of the constituent phases, i.e. WC [14] and Fe [17]. From these, and the Young's moduli calculated above, the composite Poisson's ratio is calculated using a second analytical expression from Ravichandran [18]. Finally, linear thermal expansion coefficients are taken from a previous experimental work [15]. The thermal shock parameter, calculated using equation (1), is also shown in Table 3.

Table 3
Thermal shock parameter, *R*, and constituent thermophysical properties of WC and WC-FeCr at each test temperature.

material	T (°C)	E (GPa)	α (10^{-6} K^{-1})	ν	R
WC	400	692	4.79	0.234	2.2
WC	1000	654	5.48	0.234	2.5
WC-FeCr	400	520	6.29	0.251	2.8
WC-FeCr	1000	391	8.01	0.259	0.8

Table 3 shows that the *R*-value of WC-FeCr is higher than that for WC at 400 °C. It also shows that the *R*-value for WC-FeCr degrades strongly between 400 and 1000 °C, while that of pure WC marginally increases.

We now correlate the level of damage with the *R*-value. It is expected that there would be a negative correlation between *R* and the resulting damage, as measured by the surface roughness. This expected trend is observed when looking at the effect of temperature on the WC-FeCr material: the surface roughness increases (by a factor of 9), while *R* decreases (by a factor of 3.5). The decrease in *R* is driven mainly by a loss in fracture strength (by a factor of ~3). Comparing the *R* parameters in Table 3 with surface roughness in

Fig. 4 reveals some notable exceptions to the expected trend: Firstly, in pure WC, *R* increases with increasing temperature, from 2.2 to 2.5, yet the damage extent, as measured by surface roughness, also increases by a factor of 3.5 – thus opposing the expected trend. Secondly, the differences in *R* between WC and WC-FeCr do not predict the comparative performance of each. At 400 °C, the composite shows ~25% higher *R*-value than the monolithic WC. Yet, at this temperature, the degree of surface roughness was a factor of ~6 lower and cracking far less extensive. Thus, for a given *R*-value, WC-FeCr composites damage at a much faster rate than monolithic WC ceramics. Therefore, for the materials in this study, the *R*-parameter is not a reliable one for predicting thermal shock performance. In what follows, we further consider the role of surface melting in accounting for this unreliability.

4.2. Role of localised melting

The observations of thermal shock-induced spherical pores in WC-FeCr ELM-exposed samples (Fig. 2) and large smooth, flow-like regions in disruption-exposed samples (Fig. 5) suggests that significant surface melting occurred. To estimate the surface temperature rise during a thermal shock exposure we consider a semi-infinite solid with heat flux at the surface, x=0, where the profile of temperature rise at the surface is given by [19]:

$$\Delta T = \frac{2F_0}{k}\left\{\left(\frac{Dt}{\pi}\right)^{1/2} exp\left(\frac{-x^2}{4Dt}\right) - \frac{x}{2} erfc\left(\frac{x}{2\sqrt{Dt}}\right)\right\} \quad (2)$$

Where D is the thermal diffusivity and F_0 is the surface heat flux. Although the electron beam causes volumetric heating, i.e. not pure surface heating as considered in equation (2), the beam penetration is limited to about 5 μm [6,8]. This is very small compared to the characteristic depth of thermal penetration, which, as we will show subsequently, is on the order of several hundred μm or more. The approximation of surface heating is therefore reasonable.

Fig. 8 shows the profile of ΔT at a baseline temperature of 1000 °C, for all 4 conditions investigated. WC is shown in red, and WC-FeCr in black. In all cases the temperature peaks at the surface, with a monotonically decreasing temperature that falls to below 1 K at a depth of 500 μm for the 1 ms pulses, while it falls to several hundred K for the 5 ms pulse condition at the same depth. The peak temperature rise is approximately 400-1000 °C for the 1 ms pulses, and ~6000 °C for the 5 ms pulse. In all conditions, pure WC has a slightly lower peak surface temperature than WC-FeCr, but has a slightly higher temperature at depths >100 μm. Both differences are accounted for by better heat conduction in pure WC. Also drawn on Fig. 8 are horizontal lines that represent the temperature rise required to form molten WC and a WC-FeCr eutectic at the 1000 °C test temperature, labelled ΔT_m^{WC} and ΔT_m^{FeCr} respectively, with values of ~1870 °C and ~180 °C.

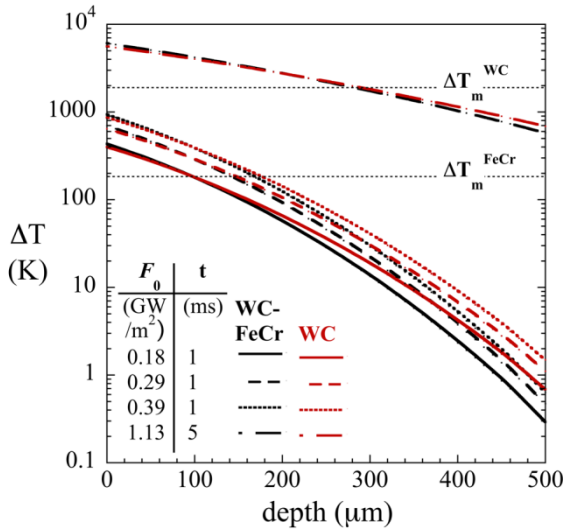

Fig. 8. temperature distribution in each phase under different heat flux conditions. The temperature rises required to form molten WC and a WC-FeCr are indicated as dotted lines.

Fig. 8 agrees well with our experimental observations after disruption event simulations. Both materials are predicted to reach the temperature required for the formation of a completely liquid phase in the near-surface region (that is, melting of the FeCr binder and WC particles in the case of WC-FeCr), as the temperature profiles exceed $\Delta T_m^{WC\text{-}FeCr}$ over the entire depth shown and exceeds ΔT_m^{WC} some ~300 μm into the depth. This prediction is in agreement with the observations of melting on a macroscopic scale in Fig. 7.

Regarding the ELM simulations, Fig. 8 also correctly predicts the discrepancy in behaviour between WC and WC-FeCr. Firstly, monolithic WC is predicted not to form a liquid phase, even at the highest power densities, as the maximum temperature rise is a factor of 2 or more below ΔT_m^{WC}. This was in agreement with Fig. 3 where no evidence of a liquid phase was found. However, Fig. 8 shows that the WC-FeCr samples would exceed ΔT_m^{FeCr} in ELM simulations, and thus form a molten phase in the near-surface region. For the 1000 °C tests this is evident from the fact that the predicted peak temperature exceeds ΔT_m^{FeCr}, in all energy conditions. This would additionally be observed for the 400 °C test, where a peak temperature rise of 940 °C is predicted, which is thus also above the threshold for melting. These predictions are in agreement with Figs 3(d-f), where nanoscale bubbles were observed in all samples.

With the above confirmation that liquid formation does indeed occur in WC-FeCr, it is interesting to revisit the apparent threshold for the onset of damage in Fig. 5(c), which was estimated to be 0.18 GW/m^2. At this level of heat flux, the surface temperature rise, calculated by Eq. 2, is predicted to be ~400 °C. This is significantly larger than ΔT_m^{FeCr}, which is ~180 °C. The difference could be attributed to two effects: the first is the localised nature of the electron beam, meaning the thermal energy supplied in a local area can diffuse into the sample more efficiently than allowed by a simple 1-dimensional heat flow model given by equation 1. The second is the enthalpy of melting for the formation of the eutectic phase, likely on the order of 10^4 kJ/mol, which, compared to its heat capacity of ~30 J/mol-K [15], equates to an adiabatic temperature rise, of $\Delta T=\Delta H_{fus}/c_p$ of 10^2-10^3 °C, meaning that even if the predicted temperature rise given by Eq. 2 exceeded the melting point by several hundred degrees, only a small fraction of the surface would actually form the liquid.

The data shown in Fig. 8 provides the basis to explain the two unexpected trends in correlating damage to the thermal shock parameter, *R*. Firstly, the fact that in ELM simulations, the WC monolith shock resistance degrades between 400 and 1000 °C, while its

R-parameter improves, can be explained by the predicted surface temperature rise of ~400-1000 °C, meaning that the thermal shock parameters calculated at the baseline temperatures will not be valid, due to large differences in thermal and mechanical properties. Secondly, the fact that at low temperature, the WC-FeCr had a better *R*-value, yet it damaged more quickly, can be explained by the fact that melting had occurred, which would lead to a dramatic loss of mechanical strength and thus a more rapid rate of damage.

Thus, it is clear that despite the promising thermal shock parameter of WC-FeCr at low temperature, its thermal shock performance is poor because the melting point of the metallic binder is always exceeded. Consequently, the relatively good shock resistance of monolithic WC is provided by its comparative thermal stability. In what follows, we compare its performance to the leading candidate plasma-facing material, W.

4.3. A comparison to rolled W

The leading candidate material for plasma-facing components in future fusion reactors is tungsten, therefore its comparison with monolithic WC is the most relevant. The performance of industrial grades of tungsten plate has been assessed also using the JUDITH 1 device [3,4]. Two particular studies have investigated materials in identical conditions to this one, that is 1000 pulses for 0.38 GW/m^2 at 400 °C and 1000 °C. The first used material from Plansee, SE, Austria [4], and the second used material provided as W monoblock mock-ups [3]. The materials were in rolled plate form with elongated grains, resulting in highly orientation-dependent properties with respect to its grain texture. Thus, three metallurgical states were investigated in each study: one with the elongated grain long-axis transverse to the surface; one with the long-axis oriented longitudinally, i.e. in the plane of the surface; and one in the recrystallised state, that is with larger equiaxed grains.

Fig. 9 compares the surface roughness of the rolled tungsten plate studies to the monolithic WC results in this study. At 400 °C, the WC displays a significantly lower roughness than any of the tungsten materials, e.g. by a factor of 2-3 for the longitudinal and transverse samples, and a factor of and 8-30 for the recrystallised samples. At 1000 °C, the advantage displayed by WC is less dramatic, showing only a factor of 2-3 improvement of the recrystallised material and a similar or slightly better surface roughness to the longitudinal and transverse materials.

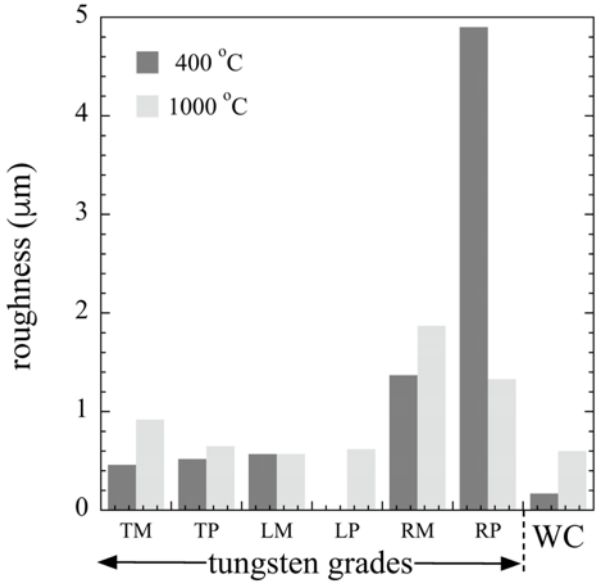

Fig. 9. comparison of the surface roughness of WC with rolled tungsten supplied in monoblock form [3] and from Plansee [4], both in various metallurgical conditions: transverse, longitudinal and

recrystallised, labelled TM, LM and RM respectively for monoblock and TP, LP and RP for Plansee material. All samples were exposed to 1000 pulses of 0.38 GW/m^2. At 400 °C, WC has a lower surface roughness than all tungsten samples.

It is possible that the higher thermal shock performance found in the WC samples compared to pure tungsten is the result of its higher strength at elevated temperature. The tensile strength of the tungsten samples was reported to be 200-350 MPa at 1000 °C [4], which can be compared to the flexural strength of the WC samples in this study, which, at 1.84 GPa, was a factor of 6-9 higher. Whilst the comparison is not as strong as it could be, because of the different loading geometries, it is supported by flexural strength data on tungsten by other authors. Palacios et al report the flexural strength of 91% dense pure tungsten at 1000 °C to be ~100 MPa [20]. Therefore, it is generally anticipated that the flexural strength of the pure tungsten samples would be lower than the WC samples used in this study.

Considering the favourable thermal shock performance of WC, it is worthwhile commenting on how the thermal shock of WC-based materials could be further improved. A key microstructural parameter is the grain size, which affects both strength and thermal conductivity. Regarding strength, it has been shown that the flexural strength of monolithic WC (with small quantities of TiC and TaC as sintering aids) can be increased from 1.3 GPa to 1.6 GPa by reducing the grain size of the powder feedstock from 5 μm to 0.6 μm [21]. Regarding thermal conductivity, it has been shown that by making carbon additions to materials processed by hot-pressing, significant grain growth can be induced, leading to increases in ambient thermal conductivity from ~110 W/m-K to ~200 W/m-K [22]. Since the dependence of conductivity and strength on grain size run counter to each other, there will be a trade-off between the two. The relationship between grain size and thermal shock resistance is therefore not easily predicted.

Finally, we note that deformation induced texture has been shown to enable improvements in thermal shock resistance in tungsten [3–5], due to an enhancement in strength within the plane of the elongated grains. It is therefore possible that such an advantageous effect could be engineering in WC. Furthermore, because of the hexagonal crystal symmetry of WC, its transport properties are anisotropic [23], meaning texture could be engineered to preferentially enhance the out-of-plane thermal conductivity, and thus minimise the overall temperature rise. Overall, further exploration of the effect of grain size and texture seems worthwhile.

5. Conclusions

Thermal shock events relevant to plasma-facing components have been simulated on candidate WC-based materials for the first time. A monolithic WC and a WC-FeCr composite were compared at various levels of heat fluence and temperature. The main conclusions were as follows:

- The thermal shock resistance of monolithic WC was higher than WC-FeCr. This result was unexpected, particularly at lower testing temperatures, because of the composite's higher thermal shock parameter.
- The unexpected behaviour was explained by melting of the FeCr metallic binder, which was confirmed by observations of melt-induced porosity in fracture surfaces and heat-flow calculations, the latter of which predict binder melting under all conditions.

- By contrast, the WC monolith was predicted to be stable with respect to melting in all ELM simulation conditions. However, in the disruption events, both materials melted on a macroscopic scale, as observed in experiments on metallic tungsten.
- Using available literature data for ELM simulations on rolled tungsten plate (1000 pulses at 0.38 GW/m^2), WC shows lower levels of damage. The difference is likely due to the comparably high fracture strength of WC at elevated temperature.

In future work, the shock performance of WC could be further improved by optimisation of the grain size, as well as the introduction of a deformation texture, the latter of which could exploit the transport anisotropy in hexagonal WC. Assessment of low cycle thermal fatigue, via transient heating events on the order ~10 s and ~10 MW/m^2, is also required.

Data availability

The raw unpublished supporting data is available on request.

Acknowledgments

The authors wish to thank Jessica Marshall and Jonathan Fair of Sandvik Hyperion for providing the WC-FeCr material and Peter Polcik of Plansee Composite Materials GmbH for providing monolithic WC. S. A. Humphry-Baker was financially supported by the Imperial College Research Fellowship.

Bibliography

[1] H. Bolt, V. Barabash, G. Federici, J. Linke, A. Loarte, J. Roth, K. Sato, Plasma facing and high heat flux materials-needs for ITER and beyond, Journal of Nuclear Materials. 307 (2002) 43–52.

[2] G. Pintsuk, A. Prokhodtseva, I. Uytdenhouwen, Thermal shock characterization of tungsten deformed in two orthogonal directions, (2011).

[3] M. Wirtz, I. Uytdenhouwen, V. Barabash, F. Escourbiac, T. Hirai, J. Linke, T. Loewenhoff, S. Panayotis, G. Pintsuk, Material properties and their influence on the behaviour of tungsten as plasma facing material, Nuclear Fusion. 57 (2017) 066018.

[4] M. Wirtz, J. Linke, T. Loewenhoff, G. Pintsuk, I. Uytdenhouwen, Thermal shock tests to qualify different tungsten grades as plasma facing material, Physica Scripta. 2016 (2016) 014015.

[5] M. Wirtz, G. Cempura, J. Linke, G. Pintsuk, I. Uytdenhouwen, Thermal shock response of deformed and recrystallised tungsten, Fusion Engineering and Design. 9 (2013) 1768–1772.

[6] I. Uytdenhouwen, M. Decréton, T. Hirai, J. Linke, G. Pintsuk, G. Van Oost, Influence of recrystallization on thermal shock resistance of various tungsten grades, Journal of Nuclear Materials. (2007) 1099–1103.

[7] G. Pintsuk, I. Uytdenhouwen, Thermo-mechanical and thermal shock characterization of potassium doped tungsten, International Journal of Refractory Metals and Hard Materials. 28 (2010) 661–668.

[8] T. Hirai, G. Pintsuk, J. Linke, M. Batilliot, Cracking failure study of ITER-reference tungsten grade under single pulse thermal shock loads at elevated temperatures, Journal of Nuclear Materials. 390 (2009) 751–754.

[9] G. Pintsuk, D. Blagoeva, J. Opschoor, Thermal shock behavior of tungsten based alloys manufactured via powder injection molding, Journal of Nuclear Materials. 442 (2013) S282–S286.

[10] G. Pintsuk, H. Kurishita, J. Linke, H. Arakawa, S. Matsuo, T. Sakamoto, S. Kobayashi, K. Nakai, Thermal shock response of fine-and ultra-fine-grained tungsten-based materials, Physica Scripta. 2011 (2011) 014060.

[11] W.E. Lee, E. Giorgi, R. Harrison, A. Maître, O. Rapaud, Nuclear Applications for Ultra-High Temperature Ceramics and MAX Phases, Ultra-High Temperature Ceramics. (2014). doi:10.1002/9781118700853.ch15.
[12] E.W. Neuman, G.E. Hilmas, W.G. Fahrenholtz, Strength of Zirconium Diboride to 2300°C, Journal of the American Ceramic Society. 96 (2013) 47–50. doi:10.1111/jace.12114.
[13] Humphry-Baker Samuel A., Smith George D. W., Shielding materials in the compact spherical tokamak, Philosophical Transactions of the Royal Society A: Mathematical, Physical and Engineering Sciences. 377 (2019) 20170443. doi:10.1098/rsta.2017.0443.
[14] R.R. Reeber, K. Wang, Thermophysical Properties of α-Tungsten Carbide, Journal of the American Ceramic Society. 82 (1999) 129–135. doi:10.1111/j.1151-2916.1999.tb01732.x.
[15] S.A. Humphry-Baker, J.M. Marshall, G.D.W. Smith, W.E. Lee, Thermophysical properties of Co-free WC-FeCr hardmetals, Proceedings of the 19th International Plansee Seminar, Reutte, Austria. (2017) HM 19.
[16] D. Hasselman, Thermal Stress Resistance of Engineering Ceramics, Materials Science and Engineering. 71 (1985) 251–264.
[17] H.J. Frost, M.F. Ashby, Deformation mechanism maps: the plasticity and creep of metals and ceramics, Pergamon press, Oxford, UK, 1982.
[18] K.S. Ravichandran, Elastic properties of two-phase composites, Journal of the American Ceramic Society. 77 (1994) 1178–1184.
[19] H.S. Carslaw, J.C. Jaeger, Conduction of heat in solids, Oxford: Clarendon Press, 1959, 2nd Ed. (1959).
[20] T. Palacios García, J.I. Pastor Caño, M.V. Aguirre Cebrian, A. Martin Sanz, M.A. Monge, A. Muñoz, R. Pareja, Mechanical behavior of tungsten-vanadium-lanthana alloys as function of temperature, Journal of Nuclear Materials. 442 (2013) S277–S281.
[21] S. Imasato, K. Tokumoto, T. Kitada, S. Sakaguchi, Properties of ultra-fine grain binderless cemented carbide 'RCCFN,' International Journal of Refractory Metals and Hard Materials. 5 (1995) 305–312.
[22] A. Gubernat, P. Rutkowski, G. Grabowski, D. Zientara, A. Gubernat, P. Rutkowski, G. Grabowski, D. Zientara, Hot pressing of tungsten carbide with and without sintering additives, International Journal of Refractory Metals and Hard Materials. (2014) 193–199.
[23] P.A. Burr, S.X. Oliver, Formation and migration of point defects in tungsten carbide: Unveiling the sluggish bulk self-diffusivity of WC, Journal of the European Ceramic Society. 39 (2019) 165–172.